Yield–stress shear thinning and shear thickening fluid flows in deformable channels

Ashish Garg[1,2] *, **Pranjal Prasad**[3]
[1]Seminare Private Limited, Delhi, India
[2]Department of Chemical Engineering, Indian Institute of Technology Delhi, India
[3]Department of Mathematics and Statistics, University of Massachusetts Amherst, MA, USA

August 25, 2023

Abstract

Yield stress shear thinning/thickening fluids flow through flexible channels, tubes are widespread in the natural world with many technological applications [1, 2, 3, 4, 5, 6, 7, 8, 9, 10, 11]. In this paper, we have derived analytical formulae for the velocity profiles and flow rate using the Herschel–Bulkley rheological model in the rigid and deformable shallow channels under lubrication approximation. To represent deformable walls, we have utilized small displacement structural mechanics and perturbation theory presented by Gervais et al. [12] and Christov et al. [13], respectively. The newly derived formulae also facilitate the flow dynamics of Newtonian fluids, power–law fluids, and Bingham fluids as its limiting cases, which have been previously derived in the literature [12, 13, 14, 15]. We find that the deformability increases the effective channel height and the flow rate in the channel. We find many scalings for the flow rate under different regimes of applied pressure and the deformability parameter. We also find that increasing the yield stress leads to a decrease in the velocity in the plug flow as well as in the non–plug flow regions. Increasing yield stress also leads to increasing the yield surface height and the solid plug in the central region due to which decreasing in the flow rate. We also find that the shear thinning/thickening index does not affect the plug height, although as the index increases, the flow rate starts to decrease due to the corresponding increase in shear thickening of the material.

Keywords: Herschel–Bulkley fluids, yield stress fluid flow, deformable channels, lubrication approximation.

1 Introduction

Herschel–Bulkley fluids are a type of non–Newtonian fluid that exhibits yield stress and their flow behavior is either shear thinning or shear thickening which are described by the Herschel–Bulkley rheological model. When these fluids flow in flexible channels, several interesting and important applications arise. Examples include in food processing where these fluids are commonly found in food products such as ketchup, mayonnaise, and yogurt. In food processing, flexible channels

*Email: **ashish.garg.iisc@gmail.com, ashish@seminare.in**

(e.g., tubes, pipes, and hoses) are used for conveying and distributing these yield stress fluids [1, 2, 3]. Understanding the flow behavior of Herschel–Bulkley fluids in flexible channels is crucial for optimizing the processing conditions, preventing blockages, and ensuring consistent product quality [4, 5, 6]. In the oil and gas industry, drilling muds and crude oil are often treated as Herschel–Bulkley fluids due to their non–Newtonian behavior. When transporting these fluids through flexible pipelines or risers, it's essential to account for their yield stress and shear thinning properties to accurately predict pressure drops and flow characteristics [7]. Herschel–Bulkley fluids are also encountered in various biomedical applications such as blood flow in vessels and transport of synovial fluid in flexible joints [8, 9]. Understanding the behaviour of such non–Newtonian fluids in flexible channels is crucial for modeling blood flow in arteries, veins and predicting flow patterns in flexible tissues [10, 11]. In polymer processing industries, such as extrusion and injection molding, Herschel–Bulkley fluids are also used. During these processes, molten polymers flow through flexible channels to form various products [16, 17, 18, 19, 20]. Waste sludges and slurries often exhibit Herschel–Bulkley behavior too. In waste management and mining industries, these materials are transported through flexible pipelines and channels [21, 22, 23, 24]. A proper understanding of their flow behavior is essential for efficient handling and processing. Some pharmaceutical formulations such as coatings, ointments, and creams, exhibit Herschel–Bulkley behavior. In pharmaceutical manufacturing processes that involve pumping and filling these formulations, understanding the flow behavior in flexible channels is crucial to ensure accurate dosing and product uniformity [25, 26, 27, 28]. Herschel–Bulkley fluids are also found in various environmental systems, such as wastewater treatment, sediment transport in rivers, and the flow of mudslides. In these scenarios, the flow behavior in flexible channels play a vital role in understanding and managing environmental processes [29, 30, 31, 32].

In the context of non–Newtonian fluids, the methods devised to handle various non–Newtonian flows in deformable conduits encounter significant analytical & numerical challenges and hence require computations [33, 34, 35, 36]. Consequently, the progress in their analytical development and utilization is hindered, and their application is limited to specific cases with notable approximations. The existing literature reveals that substantial advancements in most aspects of non–Newtonian flow in deformable conduits are lacking, leaving several research gaps where common problems remain unexplored. In the past, several endeavors have been undertaken to develop models for fluid flow in deformable conduits. The majority of these attempts have focused on Newtonian fluids, with only a few considering non–Newtonian rheologies. One well–known example of the former is the widely adopted one–dimensional (1D) Navier–Stokes flow model, specifically applied to deformable tubes in various studies [37, 38, 39, 40]. The limitation of this 1D model is that it is valid only for Newtonian flows with a large number of parameters, which makes it tough to use for any practical applications. Sochi [41] studied the flow of Newtonian and power–law fluids in elastic tubes. We note that both these models: the (1D) Navier–Stokes flow model and the model derived by Sochi [41] are not for the channel studies. Fusi et al. [42] proposed a lubrication approximation method for solving Bingham plastic flows in symmetric long channels of non–constant width. This model did not take into considerations the effects of shear thinning and shear thickening properties of the fluid. Also, it did not account for the flexibility of the channel walls. Panaseti et al. [43] extended the method of Fusi et al. [42] to solve the flow of Herschel–Bulkley fluids to include the shear thinning and shear thickening properties of the fluid with pressure–dependent consistency index and yield stress and derived analytical so-

lutions for channels with linearly varying width. However, this investigation specifically focused on rigid channel walls. Fusi and Farina [44] extended the lubrication-approximation method for axisymmetric viscoplastic flows in long tubes of varying radii assuming rigid walls of the tube. Their method has been applied by Housiadas et al. [45] to solve the flow in a tube of constant radius of a Bingham plastic with yield stress and plastic viscosity varying linearly with pressure. Fusi et al. [46] applied the method of Fusi and Farina [44] to study the flow of a Bingham plastic in tubes of varying radius, e.g. expanding or contracting tubes, or tubes with a stenosis. This model focused on tubes and did not take into account the influence of fluid characteristics that lead to shear thinning and shear thickening . Vajravelu et al. [10], have made efforts to model the flow of Herschel–Bulkley fluids in elastic tubes as a representation of non–Newtonian behavior. Vajravelu et al. [10] arrive at a broad deduction regarding the behavior of yield stress fluids within flexible tubes, wherein they ascertain that the flow rate increases with tube radius and deformability. Furthermore, they establish that both yield stress and shear thickening effects lead to a reduction in the flow rate. Nevertheless, this research, unlike our research, was conducted using tubes rather than channels. In the forthcoming results and discussions in this paper, we observe that the findings align with the generic conclusions drawn by Vajravelu et al. [10] regarding flow in tubes, which also holds for flow in channels. Moreover, we uncover more insights about the impact of shear thinning and thickening indices on plug flow, the correlation between flow rate, thinning, thickening indices, and the applied pressure at the reservoir.

In order to model flows in channels, the Poiseuille law $Q = W(-\Delta p/(12\eta L))H^3$ is indeed a significant formula in fluid dynamics, describing the relationship between the flow rate (flux) Q of a viscous incompressible fluid through a rigid tube and the pressure difference between the ends of the tube. The equation indicates that the flow rate is directly proportional to the width of the channel W, the pressure difference along the length L of the channel $\Delta p/L$, and to the cubic power of the channel height H^3. The flow rate Q is inversely proportional to the viscosity of the fluid η. A similar Poiseuille law relationship exists for rigid tubes with constant diameter and under laminar flow conditions. However, in the vascular beds of mammals, especially in the circulation of blood through arteries and arterioles, the pressure–flow relationship is non–linear, deviating from the linear behavior predicted by the Poiseuille law. This non–linearity can be attributed to several factors such as the elasticity of the walls, the non–Newtonian nature of the fluid (such as for Herschel–Bulkley or viscoelastic fluids).

The deformability of a shallow channel plays a vital role in impacting both the effective pressure drop across the channel and the resultant flow configuration [12, 13]. This is primarily because the flow rate is greatly influenced by the size of the cross–sectional dimensions, showing a strong relationship to the fourth power [13]. Consequently, even slight modifications in the geometry of the channel can lead to substantial changes in the pressure drop and flow characteristics. Gervais et al. [12] introduced a satisfactory model to explain the alteration in flow rate caused by deformations, linking a Hookean elastic response with the lubrication approximation for the Stokes flow. However, their model includes a parameter that requires empirical determination for each channel shape. Christov et al. [13] establish a connection to the parameter introduced by Gervais et al. [12] through a perturbation technique for the flow. In this study, we adopt the small displacement structural mechanics from Gervais et al. [12] and the perturbation theory as presented by Christov et al. [13] to formulate a model for a deformable channel wall for the yield stress fluid flows. Under the lubrication assumption in shallow conduits (particularly,

where the ratio of height to width and height to length are both considered small), we investigate the impact of channel flexibility on velocity profiles and the flow rate. Additionally, we analyze the influence of fluid properties such as yield stress and shear thinning/thickening index along with varying pressure conditions.

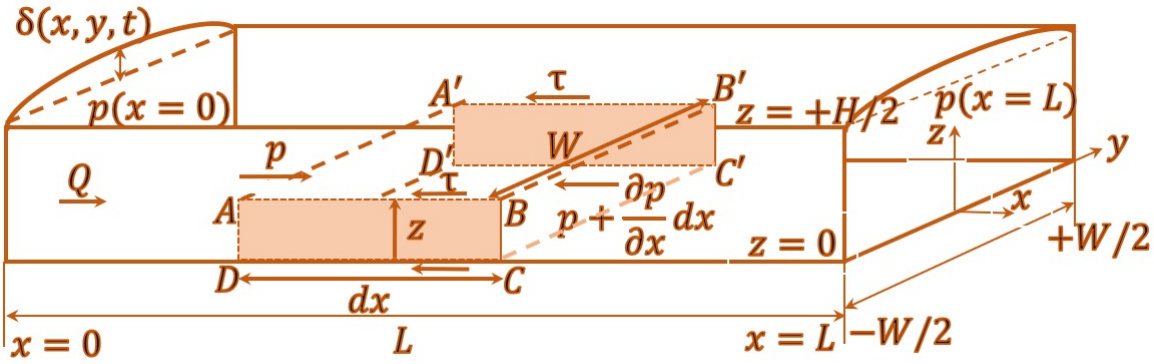

Figure 1: Schematic diagram of the upper–half part of the shallow channel of length L, cross–sectional width W, and height H. The Cartesian axis is taken at the mid–plane of the channel.

We consider a shallow rectangular channel characterized by dimensions: length L, width W, and height H, satisfying the conditions $H \ll W$ and $H \ll L$, as depicted in Figure 1. The upper surface of this channel is comprised of an elastic sheet securely attached along the edges of the vertical channel wall enabling it to undergo deformation. A pressure difference prompts a flow rate Q in the x direction. The flow's normal stresses acting on the walls cause the flexible upper wall of the channel to deform upwards in the positive z–direction, away from the $x - -y$ plane. This deformation shapes the constant configuration of the channel's top surface, represented as $z = H(x, y) = H_o + \delta(x, y)$, where $\delta(x, y)$ symbolizes the vertical deformation, as illustrated in Figure 1. At $x = 0$, a pressure field $p(x)$ is introduced at the reservoir, while the exit pressure is considered zero for reference. Presently, we abstain from assuming any specific magnitude for the displacement. However, we anticipate that, given the smallness of the pressure field, the magnitude $|\delta|$ remains significantly smaller than W within our context.

The structure of the paper is outlined as follows. Section 2 delineates the governing equations, while the Section 3 describes the model's derivation. In the Section 4, we present and analyze the results. This includes an exploration of the impact of yield stress on the necessary pressure difference to induce flow, as well as its influence on the yield surface's shape. Additionally, we probe the consequences of the shear thinning/thickening indices on both the plug and shearing velocity profiles along with the flow rate.

2 Governing equations

2.1 Cauchy equations

The Cauchy's equation and the continuity equation for an incompressible fluid are given by

$$\rho\left(\frac{\partial \boldsymbol{v}}{\partial t} + (\boldsymbol{v}\cdot\boldsymbol{\nabla})\boldsymbol{v}\right) = -\boldsymbol{\nabla}p - \rho\boldsymbol{g} + \boldsymbol{\nabla}.\boldsymbol{\tau}, \qquad \boldsymbol{\nabla}\cdot\boldsymbol{v} = 0, \tag{1a,b}$$

where $\boldsymbol{v} = [u \quad v \quad w]$ is the fluid velocity, p is the fluid pressure, ρ is the fluid density, $\boldsymbol{g}$ is the gravitational body force, and $\boldsymbol{\tau}$ is the total deviatoric stress tensor.

2.1.1 Boundary conditions

Boundary conditions play an important role in determining the solution. We assume that the fluid cannot penetrate the channel wall. Therefore, on the boundary Γ

$$\boldsymbol{v}\cdot\boldsymbol{n}_{\text{wall}} = 0, \tag{2}$$

where $\boldsymbol{n}_{\text{wall}}$ is the unit outward normal vector on the wall. We assume the no–slip boundary condition at the fluid–solid interface, which leads to

$$\boldsymbol{v}.\boldsymbol{m}_{\text{wall}} = 0, \tag{3}$$

where $\boldsymbol{m}_{\text{wall}}$ is the tangential unit vector along the channel wall. The symmetry boundary conditions at the centreline of the channel $z = 0$ demand that the velocity normal to the centreline and the velocity gradient $\boldsymbol{v_g}$ tangential to the centreline (and with in the plug) are both zero. These two conditions can be expressed as

$$\boldsymbol{v}\cdot\boldsymbol{n}_{\text{centreline}} = 0, \qquad \text{and} \qquad \boldsymbol{v_g}\cdot\boldsymbol{m}_{\text{centreline}} = 0, \tag{4a,b}$$

respectively, where $\boldsymbol{n}_{\text{centreline}}$ and $\boldsymbol{m}_{\text{centreline}}$ are the unit normal and unit tangent vector to the symmetry boundary, respectively.

3 The model

3.1 Structural mechanics: small displacement mechanics

Gervais et al. [12] performed the scaling analysis and showed that if the top wall is thick and the deformations are shallow, then the internal strains along vertical (δ/W along z direction) and lateral ($\Delta W/H$) directions are proportional to p/E, where p is the pressure and E is the elastic modulus. For $H/W \ll 1$, the strains could be rearranged to $\delta/H = cpW/EH$, where δ is the change in height due to shallow deformations and c is a unknown constant. Therefore Gervais et al. [12] approximated, the width–averaged height of the channel along the length as

$$H(x) = H_o\left(1 + \alpha\frac{p(x)W}{EH_o}\right), \tag{5}$$

where $p(x)$ is the pressure at any longitudinal direction x and $0 < \alpha < 2/3$. Young's modulus of a graphene membrane is $E = 1$ TPa. H_o is the initial height of the channel when $\delta = 0$.

However, the α is a fitting parameter that varies with the geometry of the channel and needs to be calculated explicitly from the experiments. To overcome this issue, [13] performed the perturbation analysis using the isotropic quasi–static plate bending and the Stokes equations and found that for rectangular cross–section $\alpha = (1/60)(W/\mathcal{T})^3(1-\nu^2)$, where $\mathcal{T}$ is the thickness of the upper horizontal wall and μ is the Poisson's ratio of the material (for incompressible material $\nu = 0.5$ [47]).

3.2 Herschel–Bulkley fluid model

We study the flow of yield stress, shear thinning , and thickening fluids in the flexible channels. To model the fluid behavior, we use the Herschel–Bulkley fluid model, which in one dimension is given by

$$\begin{aligned} \dot{\gamma} &= 0, \qquad \text{if} \qquad \tau < \tau_y \\ \tau &= \tau_y + \eta_o \dot{\gamma}^n, \qquad \text{if} \qquad \tau \geq \tau_y \end{aligned} \tag{6}$$

where τ and τ_y are the stress and yield stress, respectively. $\dot{\gamma}$ is the shear-rate. η_o and n are the consistency and shear-thinning/thickening indexes, respectively. If $n = 1$, the model represents the Bingham model. For $\tau_y = 0$, the model is the power–law fluid. For the cases, $n < 1$ and $n > 1$ represent the shear thinning and shear thickening fluids, respectively. Finally, $\tau_y = 0$ and $n = 1$ represents the Newtonian fluids.

3.3 2D planar model

We consider fully developed, steady laminar flow of an incompressible yield stress Hershcel–Bulkley fluid between two parallel plates under lubrication limits in a rectangular channel of height H and width W as shown schematically in Figure 1. The channel is assumed to be sufficiently long and wide in comparison to the height (that is, $H/W \ll 1$, and $H/L \ll 1$) to use a two–dimensional planar model [13, 48, 19]. We also exclude any hydrodynamic instability caused in the transience flow–field due to pulsatory pressure. We further assume a very small expansion or contraction due to deformability in comparison to the height of the channel, $\delta/H \ll 1$, which is caused by the pressure difference between the fluid and the atompheric conditions in the deformable channel. The mid–plane between the plates will be taken as the origin with the flow domain extending from $z = -H/2$ to $z = +H/2$.

Further suppose that the Cartesian velocity components u and w along longitudinal and vertical directions x and z, respectively. The z coordinate is measured from the channel's mid–plane. Therefore, using the lubrication assumptions in the shallow cross–section of the channel as shown in [13], we retain the leading order terms. Using the impermeable solid–wall boundary condition, we get $w(z = -H(x)/2) = w(z = H(x)/2) = 0$. In the leading order terms, using the impermeable solid-wall boundary condition, the normal velocity vanishes everywhere, that is,

$$w(z,t) = 0. \tag{7}$$

Further, we neglect the pressure gradient and velocity components normal to the channel wall. Also, we neglect all body forces. Under these assumptions, for $H/W \ll 1$, and $H/L \ll 1$, we show a fluid element $ABCDD'A'B'C'$ in Figure 1. The force balance on this element can be calculated as the pressure p and $p + \dfrac{\partial p}{\partial x}dx$ acting on the $AA'D'D$, and $BB'C'C$ surfaces, respectively along

the positive and negative x directions. Also, the shear stress τ_{xz} is acting along the negative x direction on both the surfaces $DD'C'C$ and $AA'B'B$. Dropping the xz notation from the stress, the force balance can be written as [15]

$$2Wpz - 2W\Big(p + \frac{\partial p}{\partial x}\, dx\Big)z = 2W\tau\, dx, \tag{8}$$

which implies

$$\tau = -\frac{\partial p}{\partial x}z, \tag{9}$$

where τ is the shear stress for the Herschel–Bulkley fluids. From equation (6), τ is given by

$$\tau = \tau_y + \eta_o\left(-\frac{\partial u}{\partial z}\right)^n, \tag{10}$$

and η_o is a Herschel–Bulkley consistency index (Bingham consistency index for $n = 1$). Using equation (9) and (10), we get

$$-\frac{\partial u}{\partial z} = \frac{1}{\eta_o^{1/n}}\left(-\frac{\partial p}{\partial x}z - \tau_y\right)^{1/n}. \tag{11}$$

Integrating equation (11), we get

$$-u = \frac{1}{\eta_o^{1/n}\left(-\frac{\partial p}{\partial x}\right)}\left(-\frac{\partial p}{\partial x}z - \tau_y\right)^{(1+n)/n} + c_1, \tag{12}$$

From equation (9), the stress on the upper channel wall is

$$\tau_{\text{wall}} = -\frac{\partial p}{\partial x}\frac{H}{2}, \tag{13}$$

Also, the yield surface H_p or the plug height below which the flow will be like a plug says that at $z = H_p$, $\dfrac{\partial u}{\partial z} = 0$. This implies from equations (9) and (10) that

$$H_p = \tau_y \Big/ \left(-\frac{\partial p}{\partial x}\right). \tag{14}$$

Using the boundary condition $u = 0$ at $z = H/2$, and equations (13) and (14) in equation (12), we get

$$u = \frac{n}{(n+1)}\frac{H}{2}\left(\frac{\tau_{\text{wall}}}{\eta_o}\right)^{1/n}\left[\left(1 - 2\frac{H_p}{H}\right)^{(1+n)/n} - \left(2\frac{z}{H} - 2\frac{H_p}{H}\right)^{(1+n)/n}\right]. \tag{15}$$

From above, the velocity in the plug that is u_p at $z = H_p$, is

$$u_p = \frac{n}{(n+1)}\frac{H}{2}\left(\frac{\tau_{\text{wall}}}{\eta_o}\right)^{1/n}\left(1 - 2\frac{H_p}{H}\right)^{(1+n)/n}. \tag{16}$$

It is important to note that the equations (15), and (16) for the flow velocities are only applicable when $H_p \leq H/2$, otherwise both the u and u_p are zero in the channel and the fluid is completely plugged without any motion. The volume flow rate in a deformable nanochannel is given by

$$Q = 2W \int_0^{H(x)/2} u \; dz = 2W \int_0^{H_p} u_p \; dz + 2W \int_{H_p}^{H(x)/2} u \; dz. \tag{17}$$

Integrating the right–hand–side of the above equation (17) and using equations (13), (14) with rearrangment, we get

$$Q = 2W \frac{n}{(2n+1)(n+1)} \left(-\frac{\partial p}{\partial x} \frac{1}{2\eta_o} \right)^{1/n} (H - 2H_p)^{(n+1)/n} \left(\frac{(n+1)H}{4} + \frac{nH_p}{2} \right). \tag{18}$$

Now, from equation (8), that

$$H(x) = H_o \left(1 + \alpha \frac{p(x)W}{EH_o} \right) = H_o \Big(1 + \beta p(x) \Big), \tag{19}$$

where $\beta = \alpha \dfrac{W}{EH_o}$. Substituting equation (19) in equation (18), we integrate along the channel length L by assuming a constant pressure gradient and a pressure $p(x)$ at x with respect to the pressure at the outlet of the channel, where we assumed the outlet pressure $p(x = L) = 0$. This yields

$$\int_x^L Q^n dx = -\left(\frac{2Wn}{(2n+1)(n+1)} \right)^n \frac{1}{2\eta_o} \int_{p(x)}^0 \Big(H_o \Big(1 + \beta p(x) \Big) - 2H_p \Big)^{n+1} \left(\frac{(n+1)H_o \Big(1 + \beta p(x) \Big)}{4} + \frac{nH_p}{2} \right)^n dp. \tag{20}$$

$$\implies Q^n (L - x) = \left(\frac{2Wn}{(2n+1)(n+1)} \right)^n \frac{1}{2\eta_o} \left[(H_o - 2H_p)^{n+1} \left(\frac{(n+1)H_o + 2nH_p}{4} \right)^n \int_0^{p(x)} \left(1 + \underbrace{\frac{\beta p(x) H_o}{(H_o - 2H_p)}}_{\mathcal{R}_1} \right)^{n+1} \left(1 + \underbrace{\frac{(n+1)H_o \beta p(x)}{(n+1)H_o + 2nH_p}}_{\mathcal{R}_2} \right)^n dp \right]. \tag{21}$$

Under small displacement assumption, where $\beta p(x) \ll 1$ such that $\mathcal{R}_1 \ll 1$, $\mathcal{R}_2 \ll 1$, therefore the expression in the integral can we approximated to the leading order of $\beta p(x)$ as

$$\left(1 + \underbrace{\frac{\beta p(x) H_o}{(H_o - 2H_p)}}_{\mathcal{R}_1} \right)^{n+1} \left(1 + \underbrace{\frac{(n+1)H_o \beta p(x)}{(n+1)H_o + 2nH_p}}_{\mathcal{R}_2} \right)^n = \left(1 + \frac{(n+1)\beta p(x) H_o}{(H_o - 2H_p)} + \frac{n(n+1)H_o \beta p(x)}{(n+1)H_o + 2nH_p} \right) + O((\beta p(x))^2) + ... \tag{22}$$

Using the leading order terms of the integral from equation (22) in equation (21), we integrate to

$$Q^n(L-x) = \left(2W\frac{n}{(2n+1)(n+1)}\right)^n \frac{1}{2\eta_o}\left[(H_o-2H_p)^{n+1}\left(\frac{(n+1)H_o+2nH_p}{4}\right)^n \left(p(x)+\frac{(n+1)\beta p^2(x)H_o}{2(H_o-2H_p)}+\frac{n(n+1)H_o\beta p^2(x)}{2(n+1)H_o+4nH_p}\right)\right]. \tag{23}$$

Using $x=0$, where $p(x)=p_{\text{in}}=-\Delta p$ (as $p_{\text{x=L}}=0$), we rewrite the above expression as

$$Q = \frac{2Wn}{(2n+1)(n+1)}\left(\frac{-\Delta p}{2\eta_o L}\right)^{1/n}\left[(H_o-2H_p)^{(n+1)/n}\left(\frac{(n+1)H_o+2nH_p}{4}\right) \underbrace{\left(1+\frac{(n+1)\beta(-\Delta p)H_o}{2(H_o-2H_p)}+\frac{n(n+1)H_o\beta(-\Delta p)}{2(n+1)H_o+4nH_p}\right)^{1/n}}_{\mathcal{X}}\right]. \tag{24}$$

It's important to emphasize that equations (24) governing the flow rate is valid exclusively when $H_p \leq H/2$. Otherwise the flow is completely chocked. We could have another asymptotic limit, where $\beta p(x) \gg 1$ such that $\mathcal{R}_1 \gg 1$, $\mathcal{R}_2 \gg 1$. In this limit, the perturbation due to flexibility is large and the predicted flow rate can have chances of large errors. Under this limit, the expression in the integral in equation (21) can be approximated to

$$\left(1+\underbrace{\frac{\beta p(x)H_o}{(H_o-2H_p)}}_{\mathcal{R}_1}\right)^{n+1}\left(1+\underbrace{\frac{(n+1)H_o\beta p(x)}{(n+1)H_o+2nH_p}}_{\mathcal{R}_2}\right)^n \approx \left(\frac{\beta p(x)H_o}{(H_o-2H_p)}\right)^{n+1}\left(\frac{(n+1)H_o\beta p(x)}{(n+1)H_o+2nH_p}\right)^n, \tag{25}$$

which gives the flow rate as

$$Q = \frac{Wn}{2(2n+1)}\left(\frac{(-\Delta p)^{2n+2}}{2\eta_o L(2n+2)}\right)^{1/n}\left[\left(\beta H_o\right)^{(2n+1)/n}\right]. \tag{26}$$

3.4 Limiting cases

3.4.1 For the Bingham fluid flow in flexible channel: $n=1$

Using equation (24) under the small displacement assumption for the Bingham fluid flow, that is, $n=1$, we get

$$Q = \frac{W}{12}\left(\frac{-\Delta p}{\eta_o L}\right)\left[\left(H_o-2H_p\right)^2\left(H_o+H_p\right)\left(1+\frac{\beta(-\Delta p)H_o}{(H_o-2H_p)}+\frac{H_o\beta(-\Delta p)}{2H_o+2H_p}\right)\right]. \tag{27}$$

To the best of our knowledge, we have not seen the above derived equation (27) in the literature so far.

3.4.2 For the Newtonian fluid flow in flexible channel: $n = 1$, $H_p = 0$

Similarly, using equation (24) under the small displacement assumption for the Newtonian fluid flow, that is, $n = 1$, $\tau_y = 0 \implies H_p = 0$, we get

$$Q = \frac{W}{12}\left(\frac{-\Delta p}{\eta_o L}\right) H_o^3 \left(1 + \frac{3\beta(-\Delta p)}{2}\right). \tag{28}$$

The above expression (28) is also derived by Gervais et al. [12], Christov et al. [13], Garg [14] for $\beta|\Delta p| \ll 1$.

3.4.3 For the Herschel–Bulkley fluid flow in the rigid channel: $\beta = 0$

Using equation (24) under the small displacement assumption for the Herschel–Bulkley fluid flow in the rigid channel, that is, $\beta = 0$, we get

$$Q = \frac{2Wn}{(2n+1)(n+1)}\left(\frac{-\Delta p}{2\eta_o L}\right)^{1/n}\left[\Big(H_o - 2H_p\Big)^{(n+1)/n}\left(\frac{(n+1)H_o + 2nH_p}{4}\right)\right]. \tag{29}$$

A similar expression but for the Bingham fluid flow in rigid channel is given in Chhabra and Richardson [15].

3.4.4 For the Bingham fluid flow in the rigid channel: $\beta = 0$, $n = 1$

Using equation (24) for the Bingham fluid flow in the rigid channel, we get

$$Q = \frac{W}{12}\left(\frac{-\Delta p}{\eta_o L}\right)\Big(H_o - 2H_p\Big)^2\Big(H_o + H_p\Big), \tag{30}$$

which is also given in Chhabra and Richardson [15].

3.4.5 For the power–law fluid flow in the rigid channel: $\beta = 0$, $\tau_y = 0$

Using equation (24), for the power–law fluid flow in the rigid channel, we get

$$Q = \frac{H_o W n}{(2n+1)}\left(\frac{1}{2}\right)^{(1+n)/n}\left(\frac{-\Delta p}{\eta_o L}\right)^{1/n}\Big(H_o\Big)^{(n+1)/n}, \tag{31}$$

which is also given in Chhabra and Richardson [15].

3.4.6 For the Newtonian fluid flow in the rigid channel: $\beta = 0$, $n = 1$, $H_p = 0$

Using equation (24) for the Newtonian fluid flow in the rigid channel, we get

$$Q = \frac{W}{12}\left(\frac{-\Delta p}{\eta_o L}\right) H_o^3, \tag{32}$$

which is a classical result of the Hagen–Poiseuille flow in channels as given in [49, 50, 51, 15, 14].

4 Results and discussion

4.1 Effect of yield stress on the flow in the rigid and deformable channel

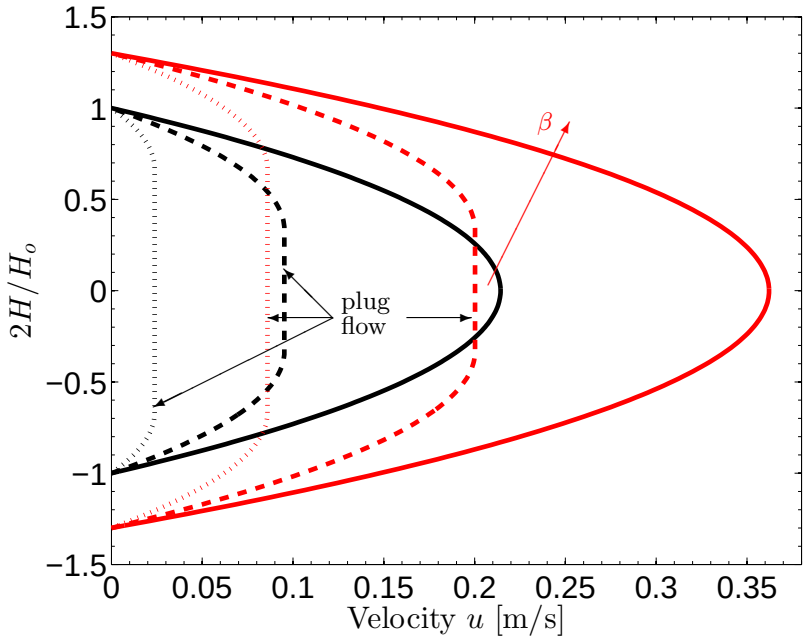

Figure 2: Velocity profiles at varying yield stress for the rigid ($\beta = 0$, in black) and deformable ($\beta = 0.005$, in red) channels. The solid line, dashed line, and dotted lines show the data at yield stress values of 0 Pa, 2 Pa, and 4 Pa, respectively.

For the discussions in the results section, we set $H_o = 0.1$ m, $L = 0.5$ m, $W = 1$ m, and $\eta_o = 0.7$ Pa everywhere. From equation (14), we calculate the values of plug height as $H_p = \tau_y L/|\Delta p|$. Using equations (15) (for $z > H_p$) and (16) (for $0 \leq z \leq H_p$), we show the velocity profiles at $|\Delta p| = 60$ Pa, $n = 1$ at varying yield stress for the rigid ($\beta = 0$ Pa^{-1}, in the black color), and deformable ($\beta = 0.005$ Pa^{-1}, in the red color) channels in Figure 2. The solid line, dashed line, and dotted lines show the data at yield stress values of $\tau_y = 0$ Pa, $\tau_y = 2$ Pa, and $\tau_y = 4$ Pa, respectively. We find that due to flexibility ($\beta = 0.005$ Pa^{-1}) in the channel, the channel height increases by 30%.

Further for $\tau_y = 0$ Pa, we find that the deformability parameter increases from 0 to 0.005 Pa^{-1}. The maximum velocity at the centerline increases from approximately 0.21 m/s to 0.36 m/s. This trend has been found at non–zero yield stress values too. In the presence of yield stress, the velocity profiles are divided into two parts, the plug velocity within the central region where the bulk of the fluid moves with a constant velocity as a solid material. On the other hand, for $z > H_p$, the velocity profile is dictated as the fluid is flowing normally with finite shear stresses. We find that for $\tau_y = 2$ Pa, the centerline plug velocity increases from 0.09 m/s in the rigid channel to 0.19 m/s in the deformable channel with $\beta = 0.005$ Pa^{-1} as shown with dashed black and red lines respectively. A similar increment due to deformation is found at $\tau_y = 4$ Pa. This indicates that the deformability increases the velocity and hence the flow rate in the deformable channel for a given pressure and material properties. We also find that as the yield stress is

increasing, the plug height keeps increasing and the maximum velocity decreases which also decreases the flow rate in the channel.

4.2 Effect of shear-thinning/thickening on the flow in the rigid and deformable channel

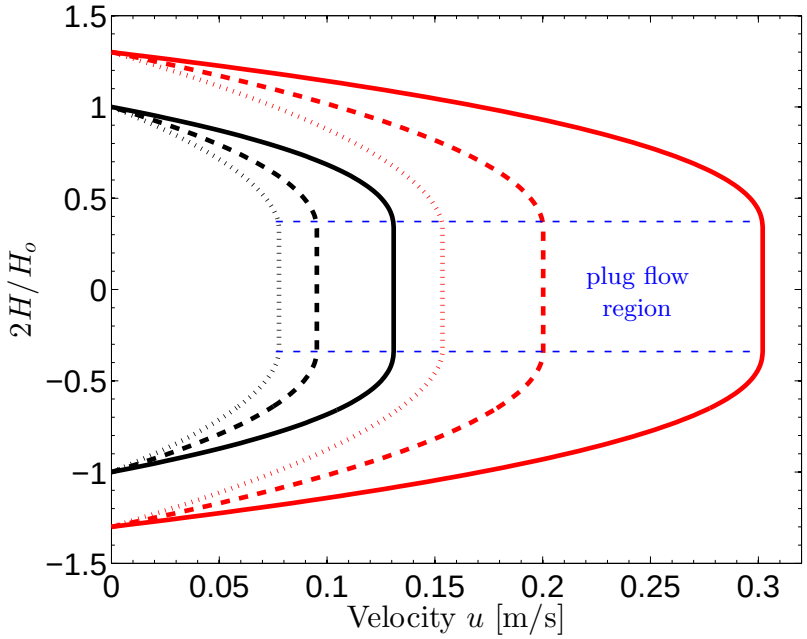

Figure 3: Velocity profiles at varying shear thinning and thickening index for the rigid ($\beta = 0$, in black) and deformable ($\beta = 0.005$, in red) channels. The solid line, dashed line, and dotted lines show the data at shear thinning/thickening index values of $n = 0.8$, $n = 1$, and $n = 1.2$, respectively. The central region within the dashed blue line indicates the plug flow region.

We show the velocity profiles at $|\Delta p| = 60$ Pa, $\tau_y = 2$ Pa at varying shear thinning/thickening index n for the rigid ($\beta = 0$ Pa^{-1}, in the black color), and deformable ($\beta = 0.005$ Pa^{-1}, in the red color), channels in Figure 3. The solid line, dashed line, and the dotted lines show the data at shear thinning/thickening index n of $n = 0.8$, $n = 1$, and $n = 1.2$, respectively. The central region within the dashed blue line indicates the plug flow region.

We find that due to non–zero yield stress in all predictions, the velocity profiles are divided into two parts, the plug velocity in the central region and the normal shearing velocity towards the channel wall. For $n = 1$ (Bingham fluid), as the deformability parameter increases from 0 to 0.005 Pa^{-1}. The maximum velocity at the centerline increases from approximately 0.09 m/s to 0.2 m/s as shown with dashed lines. This trend has been found in shear thinning ($n = 0.8$), and shear thickening ($n = 1.2$) materials too. We find that for $n = 0.8$, the centerline plug velocity increases from 0.12 m/s in the rigid channel to 0.3 m/s in the deformable channel with $\beta = 0.005$ Pa^{-1} as shown with solid black and red lines respectively. A similar increment due to deformation is found for $n = 1.2$. This indicates that the deformability increases the velocity and hence the flow rate in the deformable channel for a given pressure and material properties. We

also find that as the shear thinning/thickening index n is increasing, although the plug height remains the same but the maximum velocity decreases which also decreases the flow rate in the channel.

4.3 Effect of yield stress and shear thinning/thickening index on the flow rate in the rigid channel

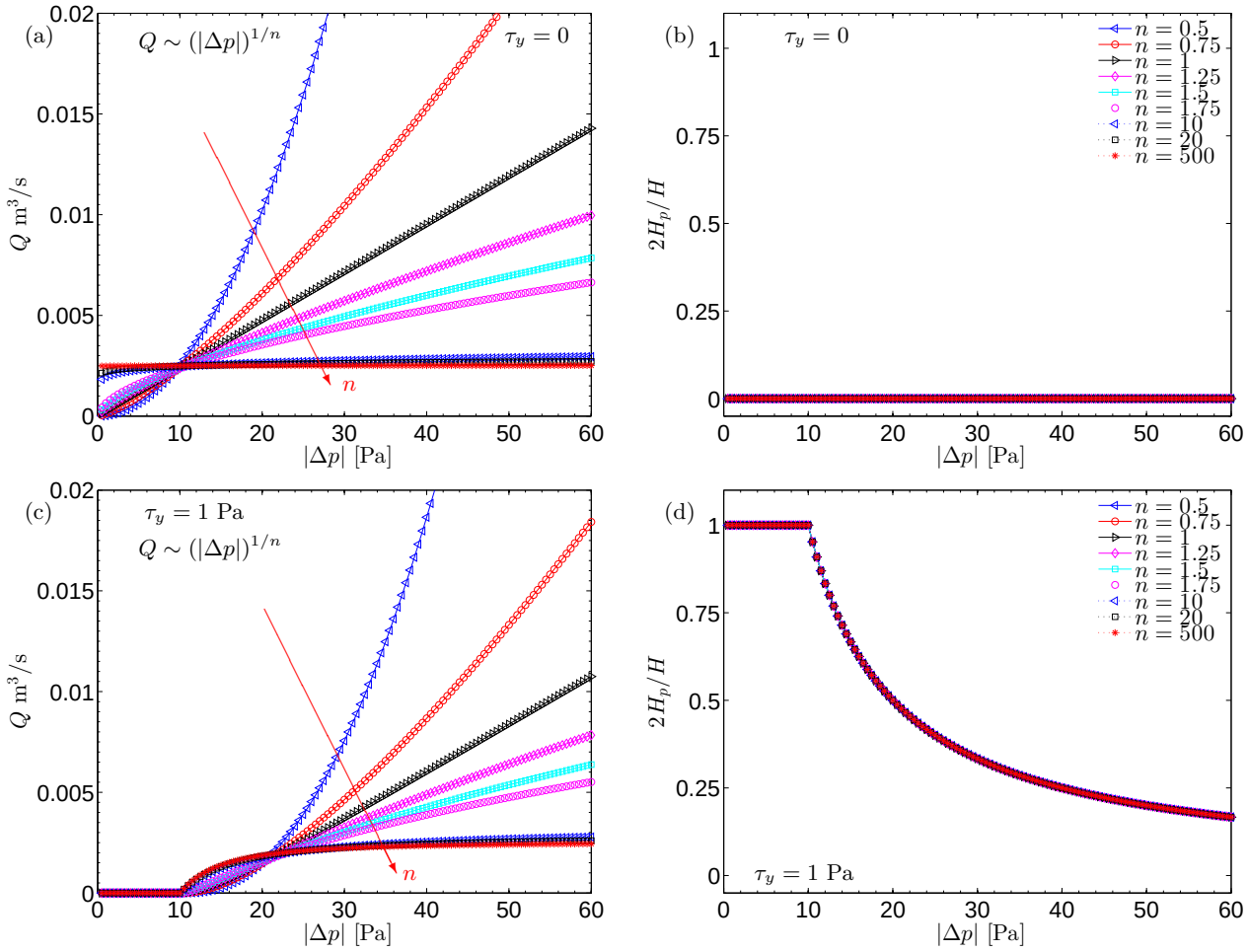

Figure 4: We show the flow rate in the rigid ($\beta = 0$ Pa^{-1}) channel at varying $|\Delta p|$, and shear thinning/thickening index n at $\tau_y = 0$ Pa in (a), and $\tau_y = 1$ Pa in (c), respectively. The red arrow indicates the increasing values of shear thinning/thickening index n with 0.5, 0.75, 1, 1.25, 1.5, 1.75, 10, 20, and 500 from blue triangle to red circles, respectively. In Figures (b) and (d), we show the corresponding plug height with varying pressure for all n at $\tau_y = 0$ Pa, and $\tau_y = 1$ Pa, respectively.

Using equation (24), we calculate the flow rate in the rigid ($\beta = 0$ Pa^{-1}) channel at varying $|\Delta p|$, and shear thinning/thickening index n at $\tau_y = 0$ Pa in Figure 4(a), and $\tau_y = 1$ Pa in Figure 4(c), respectively. The red arrow indicates the increasing values of shear thinning/thickening index n with 0.5, 0.75, 1, 1.25, 1.5, 1.75, 10, 20, and 500 from blue triangle to red circles, respectively. We find that for $n < 1$, the flow rate curve is like an upward parabola, whereas for

$n = 1$, it is a straight line and $n > 1$, it is a rightward parabola. Due to that, for $|\Delta p| \leq 10$ Pa, the flow rate for $n < 1$, is lower than for $n > 1$, whereas it becomes the opposite for $|\Delta p| > 10$ Pa. In the case of a rigid channel wall, the flow rate scales as $Q \sim (|\Delta p|)^{1/n}$. We find that for $n = 10,\ 20$, the Q is weakly dependent on $|\Delta p|$, further as the $n \gg 1$ such as for $n = 500$ (shown with red asterisk), the flow rate becomes independent to $|\Delta p|$. This behaviour is consistent with the scaling also, where $Q \sim (|\Delta p|)^{1/n}$ and as $n \implies \infty$, $Q \sim (|\Delta p|)^0$. In Figure 4(b), we show the corresponding plug height with varying pressure for all n. We find that, for $\tau_y = 0$ Pa, the $H_p = 0$ for all n and the data collapse on the same line.

On the other hand for $\tau_y = 1$ Pa in Figure 4(c), We find that below $|\Delta p| = 10$ Pa, $H_p = H_o/2$, thus the material inside the channel is plugged and can not flow, hence show no flow rate. As the pressure difference increases, the flow rate starts to build and show similar trends as in Figure 4(a). We also find that, for given $|\Delta p|$, and n, the flow rate decreases as yield stress is increased. We show the corresponding plug height at $\tau_y = 1$ Pa with varying pressure for all n in Figure 4(d). We find that the plug height H_p collapse on the same curve for all n. We find that for $\tau_y = 1$ Pa, $H_p = H_o/2$ for $|\Delta p| \leq 10$ Pa. As the pressure increases the H_p monotonically decreases as $H_p \sim |\Delta p|^{-1}$, which is consistent with equation (14). We also find that the shear thinning/thickening index does not affect the plug height which is also consistent with what we saw in the velocity profiles in the previous section 4.2.

4.4 Effect of yield stress and shear-thinning/thickening index on the flow rate in the deformable channel

We calculate the flow rate in the deformable ($\beta = 0.005$ Pa^{-1}) channel at varying $|\Delta p|$, and shear thinning/thickening index n at $\tau_y = 0$ Pa in Figure 5(a), and $\tau_y = 1$ Pa in Figure 5(c), respectively. The red arrow indicates the increasing values of shear thinning/thickening index n with 0.5, 0.75, 1, 1.25, 1.5, 1.75, 10, 20, and 500 from blue triangle to red circles, respectively. We find that for $n \leq 1.25$, the flow rate curve is like an upward parabola, whereas for $n > 1.25$, it is a rightward parabola. Due to that, for $|\Delta p| \leq 10$ Pa, the flow rate for $n \leq 1.25$, is lower than for $n > 1.25$, whereas it becomes opposite for $|\Delta p| > 10$ Pa. In case of deformable wall channel, the flow rate scales as $Q \sim (|\Delta p|)^{1/n}$ for $\mathcal{X} \lesssim O(10^{-1})$ (the $\mathcal{X}$, which is shown as the under–brace term in equation (24). On the other hand the flow rate scales as $Q \sim (|\Delta p|)^{2/n}$ for $\mathcal{X} \sim O(10^0)$. We truncated our expansion in equation (23) because of the small displacement deformability, otherwise for much larger pressure, we need to take those terms into account which gives the scaling as $Q \sim (|\Delta p|)^{2+2/n}$ as shown in equation (26) (although the theory could predict large errors in this asymptotic limit. For $n = 1$, we find that the flow rate $Q \sim (|\Delta p|)^4$, which is consistent as found in [13, 12, 14]). In Figure 5(b), we show the corresponding plug height with varying pressure for all n. Also, for $\tau_y = 0$ Pa, $H_p = 0$.

On the other hand for $\tau_y = 1$ Pa in Figure 5(c), we find that below $|\Delta p| = 10$ Pa, $H_p = H/2$, thus the material inside the channel is plugged and can not flow, hence show no flow rate. As the pressure difference increases, the flow rate starts to build and show similar trends as in Figure 5(a). We also find that for given $|\Delta p|$, and n, the flow rate decreases as yield stress is increased. We show the corresponding plug height at $\tau_y = 1$ Pa with varying pressure for all n in Figure 5(d). We find that for $\tau_y = 1$ Pa, $H_p = H_o/2$ for $|\Delta p| \leq 6.5$ Pa. As the pressure increases, H_p monotonically decreases as $H_p \sim |\Delta p|^{-1}$. We also find that in the case of the deformable

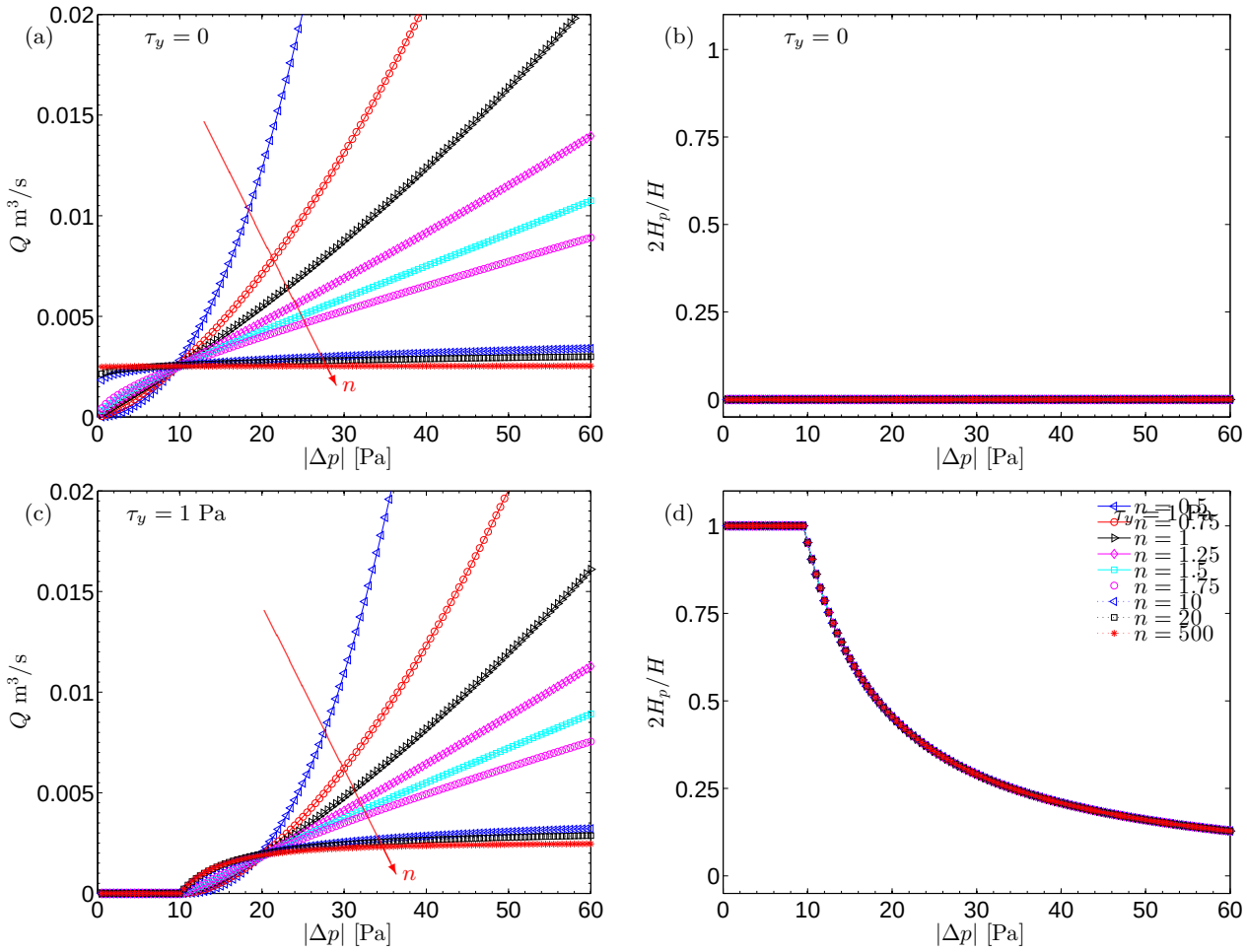

Figure 5: We show the flow rate in the deformable ($\beta = 0.005$ Pa^{-1}) channel at varying $|\Delta p|$, and shear thinning/thickening index n at $\tau_y = 0$ Pa in (a), and $\tau_y = 1$ Pa in (c), respectively. The red arrow indicates the increasing values of shear thinning/thickening index n with 0.5, 0.75, 1, 1.25, 1.5, 1.75, 10, 20, and 500 from blue triangle to red circles, respectively. In Figures (b), and (d), we show the corresponding plug height with varying pressure for all n at $\tau_y = 0$ Pa and $\tau_y = 1$ Pa, respectively.

channel as well, the shear thinning/thickening index does not affect the plug height which is also consistent with what we saw in the velocity profiles in the previous section 4.2. On comparison of Figure 4(a,c), and 5(a,c), we further find that at given pressure and material properties, due to deformability the flow rate increases.

5 Conclusion

In this paper, we derived analytical formulae for the velocity profiles and volumetric flow rate in the rigid and deformable channels for the shear thinning and shear thickening yield stress materials. We focus on investigating the impact of many factors such as the deformability of the channel wall, yield stress, shear thinning, and shear thickening index. In these derivations, we used the small displacement structural mechanics and perturbation theory presented by Gervais

et al. [12], and Christov et al. [13], respectively for the constitutive relations of the elastic nature of the channel–walls. We assumed the lubrication assumption in the shallow channels, where the flow velocity profile is assumed to be determined locally by the fluid rheology and the size of the local cross–sectional area. The newly derived formulae facilitate the flow dynamics of Newtonian fluids, power–law fluids, Bingham fluids, and shear thinning and thickening yield stress fluids as its limiting cases. For validation, several sensible trends have been observed. These include (a) the exact derived expression to their corresponding rigid channel–wall formulas given in literature [12, 13, 14, 15] for the Bingham fluids, power–law fluids and the Newtonian fluids. Thorough tests have revealed that the newly derived formulae produce mathematically and physically sensible results in diverse situations of fluid rheology, shallow channel geometry, and boundary conditions. The derivation method proposed in this paper can in principle be extended to less regular geometries (e.g. converging-diverging) or regular geometries such as tubes.

We also examined the influence of the deformability of the wall on the the behavior of non–Newtonian yield stress flows within the channels. We found that the deformability increases the effective channel height and the flow rate in the channel. In case of deformable wall channel, the flow rate scales as $Q \sim (|\Delta p|)^{1/n}$ for $\mathcal{X} \lesssim O(10^{-1})$ (the $\mathcal{X}$ is shown as the under–brace term in equation (26)), on the other hand the flow rate scales as $Q \sim (|\Delta p|)^{2/n}$ for $\mathcal{X} \sim O(10^{0})$. Further, for the large perturbations, the flow rate scales as $Q \sim (|\Delta p|)^{2+2/n}$ (although the theory could predict large errors in this asymptotic limit, and for $n = 1$, we find that the flow rate $Q \sim (|\Delta p|)^4$, which is consistent as found in [13, 12, 14]). It is known that due to the presence of yield stress, a threshold inlet pressure is required for the onset of flow in the channels unlike in the case of the Newtonian or power–law fluids. We find that below this threshold, the flow is chocked in the channels with plug height the same as the channel height, that is, $H_p = \pm H_o/2$. We also find that increasing yield stress leads to decreases in the velocity in the plug flow as well as in the non–plug flow regions. Increasing yield stress also leads to increasing the yield surface height and the solid plug in the central region due to decreasing the flow rate. We also find that the shear thinning index does not affect the plug height, although as the index increases the flow rate starts to decrease due to corresponding more shear thickening of the material.

References

[1] N Singla, P Verma, G Ghoshal, and S Basu. Steady state and time dependent rheological behaviour of mayonnaise (egg and eggless). *International Food Research Journal*, 20(4):2009, 2013.

[2] Qixin Zhong and Christopher R Daubert. Food rheology. In *Handbook of farm, dairy and food machinery engineering*, pages 403–426. Elsevier, 2013.

[3] GHR Kefayati and RR Huilgol. Lattice boltzmann method for the simulation of the steady flow of a bingham fluid in a pipe of square cross-section. *European Journal of Mechanics-B/Fluids*, 65:412–422, 2017.

[4] Pamela Anne Cole. *Cleaning of toothpaste from process equipment by fluid flow at laboratory and pilot scales*. PhD thesis, University of Birmingham, 2013.

[5] Anne-Laure Vayssade. *Flows of Herschel-Bulkley fluids in confined environments: applications to the cementing of oil wells*. PhD thesis, Université Pierre et Marie Curie-Paris VI, 2015.

[6] Samira Baba Hamed. Optimizing the transport of cuttings with ecological drilling muds: application to directional well. *Journal of the Brazilian Society of Mechanical Sciences and Engineering*, 42(12):619, 2020.

[7] Jason Maxey. Thixotropy and yield stress behavior in drilling fluids. In *AADE 2007 drilling fluids conference (AADE-07-NTCE-37)*, 2007.

[8] K Das. A mathematical model on the consistency coefficient of the herschel–bulkley flow of blood through narrow vessel. *Arabian Journal for Science and Engineering*, 36:405–413, 2011.

[9] Amit Bhatnagar and RK Shrivastav. Analysis of mhd flow of blood through a multiple stenosed artery in the presence of slip velocity. *International Journal of Innovative Research in Advanced Engineering (IJIRAE)*, 1(10):250–257, 2014.

[10] Kuppalapalle Vajravelu, Sreedharamalle Sreenadh, Palluru Devaki, and Kerehalli Prasad. Mathematical model for a herschel-bulkley fluid flow in an elastic tube. *Open Physics*, 9(5):1357–1365, 2011.

[11] G Neeraja, PA Dinesh, K Vidya, and CSK Raju. Peripheral layer viscosity on the stenotic blood vessels for herschel-bulkley fluid model. *Informatics in Medicine Unlocked*, 9:161–165, 2017.

[12] Thomas Gervais, Jamil El-Ali, Axel Günther, and Klavs F Jensen. Flow-induced deformation of shallow microfluidic channels. *Lab on a Chip*, 6(4):500–507, 2006.

[13] Ivan C Christov, Vincent Cognet, Tanmay C Shidhore, and Howard A Stone. Flow rate–pressure drop relation for deformable shallow microfluidic channels. *Journal of Fluid Mechanics*, 841:267–286, 2018.

[14] Ashish Garg. Pulsatile pressure enhanced rapid water transport through flexible graphene nano/angstrom-size channels: A continuum modelling approach using the micro-structure of nanoconfined water. *ChemRxiv DOI: 10.26434/chemrxiv-2023-hlw5q*, 2023.

[15] Raj P Chhabra and John Francis Richardson. *Non-Newtonian flow and applied rheology: engineering applications*. Butterworth-Heinemann, 2011.

[16] John J McKetta. *Encyclopedia of Chemical Processing and Design: Volume 37-Pipeline Flow: Basics to Piping Design*. Routledge, 2022.

[17] KP Akshay Kumar, Miroslav Černík, and Vinod VT Padil. Recent advances in tree gum polymers for food, energy, and environmental domains. *Progress in Polymer Research for Biomedical, Energy and Specialty Applications*, pages 95–117, 2022.

[18] NS Deshpande and M Barigou. Vibrational flow of non-newtonian fluids. *Chemical Engineering Science*, 56(12): 3845–3853, 2001.

[19] Ashish Garg, Nico Bergemann, Beccy Smith, Matthias Heil, and Anne Juel. Fluidisation of yield stress fluids under vibration. *Science Talks*, 3:100067, 2022.

[20] Ashish Garg. Fluidisation of yield stress materials under vibration. *PhD thesis, The University of Manchester*, pages 1–175, 2022.

[21] Ali Faghani, Samya Sen, Mahdi Vaezi, and Amit Kumar. Rheology of fibre suspension flows in the pipeline hydro-transport of biomass feedstock. *Biosystems Engineering*, 200:284–297, 2020.

[22] Weiqi Fu, Zhiyuan Wang, Baojiang Sun, Jianchun Xu, Litao Chen, and Xuerui Wang. Rheological properties of methane hydrate slurry in the presence of xanthan gum. *SPE Journal*, 25(05):2341–2352, 2020.

[23] Dhruv Mehta, Adithya Krishnan Thota Radhakrishnan, Jules Van Lier, and Francois Clemens. A wall boundary condition for the simulation of a turbulent non-newtonian domestic slurry in pipes. *Water*, 10(2):124, 2018.

[24] Ashish Garg, Nico Bergemann, Beccy Smith, Matthias Heil, and Anne Juel. Fluidisation of yield stress fluids under vibration. *Journal of Non-Newtonian Fluid Mechanics*, 294:104595, 2021.

[25] Chi H Lee, Venkat Moturi, and Yugyung Lee. Thixotropic property in pharmaceutical formulations. *Journal of controlled release*, 136(2):88–98, 2009.

[26] Ozge Inal, Gulin Amasya, Zerrin Sezgin Bayindir, and Nilufer Yuksel. Development and quality assessment of glutathione tripeptide loaded niosome containing carbopol emulgels as nanocosmeceutical formulations. *International Journal of Biological Macromolecules*, 241:124651, 2023.

[27] Christopher Marriott. Viscosity, rheology and the flow of fluids. *Aulton's Pharmaceutics E-Book: The Design and Manufacture of Medicines*, page 94, 2013.

[28] Vidit Sharma and Ashish Garg. Numerical investigation of effects of compound angle and length to diameter ratio on adiabatic film cooling effectiveness. *CoRR*, abs/1405.0560, 2014. URL `http://arxiv.org/abs/1405.0560`.

[29] Nayeli Gutiérrez-Casiano, Eduardo Hernández-Aguilar, Alejandro Alvarado-Lassman, and Juan M Méndez-Contreras. Removal of carbon and nitrogen in wastewater from a poultry processing plant in a photobioreactor cultivated with the microalga chlorella vulgaris. *Journal of Environmental Science and Health, Part A*, 57(7):620–633, 2022.

[30] Rida Elgaddafi, Ramadan Ahmed, and Fred Growcock. Settling behavior of particles in fiber-containing herschel bulkley fluid. *Powder Technology*, 301:782–793, 2016.

[31] Renfu Xu, Yahui Feng, Qihui He, Wenxun Yan, Min Yuan, and Baixing Hu. Review and perspectives of anionic dispersants for coal–water slurry. *Energy & Fuels*, 37(7):4816–4834, 2023.

[32] Shielan Liu and Michael Henderson. An overview on methodologies for tailings dam breach study. In *Proceeding of the Twenty-Fourth International Conference on Tailings and Mine Waste*, 2020.

[33] Prashanta Kumar Mandal. An unsteady analysis of non-newtonian blood flow through tapered arteries with a stenosis. *International journal of non-linear mechanics*, 40(1):151–164, 2005.

[34] S Sreedharamalle, D Palluru, and D Reddy. Krishnaiah. unsteady flow of a jeffrey fluid in an elastic tube with a stenosis. In *Proceedings of the International Conference on Fluid Dynamics and Thermodynamics Technologies*, volume 33, page 1, 2012.

[35] Praveen Chandrashekar and Ashish Garg. Vertex-centroid finite volume scheme on tetrahedral grids for conservation laws. *Computers & Mathematics with Applications*, 65(1):58–74, 2013.

[36] Shivam Singhal, Yayati Gupta, and Ashish Garg. Fluid dynamics android application: An efficient semi-implicit solver for compressible flows. 2019.

[37] ACL Barnard, WA Hunt, WP Timlake, and E Varley. A theory of fluid flow in compliant tubes. *Biophysical journal*, 6(6):717–724, 1966.

[38] Mette S Olufsen. A one-dimensional fluid dynamic model of the systemic arteries. In *Computational Modeling in Biological Fluid Dynamics*, pages 167–187. Springer, 2001.

[39] NP Smith, AJ Pullan, and Peter J Hunter. An anatomically based model of transient coronary blood flow in the heart. *SIAM Journal on Applied mathematics*, 62(3):990–1018, 2002.

[40] SJ Sherwin, V Franke, J Peiró, and K20389821200 Parker. One-dimensional modelling of a vascular network in space-time variables. *Journal of engineering mathematics*, 47:217–250, 2003.

[41] Taha Sochi. The flow of newtonian and power law fluids in elastic tubes. *International Journal of Non-Linear Mechanics*, 67:245–250, 2014.

[42] Lorenzo Fusi, Angiolo Farina, Fabio Rosso, and Sabrina Roscani. Pressure driven lubrication flow of a bingham fluid in a channel: A novel approach. *Journal of Non-Newtonian fluid mechanics*, 221:66–75, 2015.

[43] Pandelitsa Panaseti, Yiolanda Damianou, Georgios C Georgiou, and Kostas D Housiadas. Pressure-driven flow of a herschel-bulkley fluid with pressure-dependent rheological parameters. *Physics of fluids*, 30(3), 2018.

[44] Lorenzo Fusi and Angiolo Farina. Peristaltic axisymmetric flow of a bingham fluid. *Applied Mathematics and Computation*, 320:1–15, 2018.

[45] Kostas D Housiadas, Iasonas Ioannou, and Georgios C Georgiou. Lubrication solution of the axisymmetric poiseuille flow of a bingham fluid with pressure-dependent rheological parameters. *Journal of Non-Newtonian Fluid Mechanics*, 260:76–86, 2018.

[46] Lorenzo Fusi, Kostas D Housiadas, and Georgios C Georgiou. Flow of a bingham fluid in a pipe of variable radius. *Journal of Non-Newtonian Fluid Mechanics*, 285:104393, 2020.

[47] Peter H Mott, John R Dorgan, and CM Roland. The bulk modulus and poisson's ratio of "incompressible" materials. *Journal of Sound and Vibration*, 312(4-5):572–575, 2008.

[48] Ashish Garg. Aerodynamics. In *GATE Aerospace Forum Educational Services*, 2015.

[49] Frank M White. *Fluid mechanics*. New York, 1990.

[50] George Keith Batchelor. *An introduction to fluid dynamics*. Cambridge university press, 1967.

[51] Brian J Kirby. *Micro-and nanoscale fluid mechanics: transport in microfluidic devices*. Cambridge university press, 2010.